

# Temperature-dependent electron and phonon dynamics in the ternary topological insulator $(\text{Bi}_{1-x}\text{Sb}_x)_2\text{Te}_3$ at terahertz frequencies

Alexander Stroh<sup>1</sup>, Hassan A. Hafez<sup>1,\*</sup>, Pascal Strathkötter<sup>1</sup>, Andrew D. Burnett<sup>3</sup>, John Kendrick<sup>3</sup>, Alessandra Di Gaspare<sup>4</sup>, Maik Gärner<sup>1</sup>, Judith Bünthe<sup>1</sup>, Chiara Seidel<sup>1</sup>, Ahmet Yagmur<sup>4</sup>, Craig S. Knox<sup>2,4</sup>, Matthew Vaughan<sup>2</sup>, Nathan Fox<sup>2</sup>, Satoshi Sasaki<sup>4</sup>, Andreas Hütten<sup>1</sup>, Edmund Linfield<sup>2</sup>, Miriam S. Vitiello<sup>5</sup>, Joshua Freeman<sup>2</sup>, and Dmitry Turchinovich<sup>1,†</sup>


<sup>1</sup>Fakultät für Physik, *Universität Bielefeld*, Universitätsstr. 25, 33615 Bielefeld, Germany

<sup>2</sup>School of Electronic and Electrical Engineering, *University of Leeds*, West Yorkshire LS2 9JT, United Kingdom

<sup>3</sup>School of Chemistry, *University of Leeds*, West Yorkshire LS2 9JT, United Kingdom

<sup>4</sup>School of Physics and Astronomy, *University of Leeds*, West Yorkshire LS2 9JT, United Kingdom

<sup>5</sup>NEST, *CNR-Istituto Nanoscienze and Scuola Normale Superiore* Piazza San Silvestro 12, Pisa 56127, Italy

 (Received 20 May 2025; revised 24 September 2025; accepted 20 October 2025; published 1 December 2025)

We investigate the temperature-dependent free electron conduction, terahertz phonon modes, and electron-phonon interactions, in the ternary topological insulator  $(\text{Bi}_{1-x}\text{Sb}_x)_2\text{Te}_3$ . Terahertz time-domain spectroscopy and Raman spectroscopy on three *n*-type  $(\text{Bi}_{1-x}\text{Sb}_x)_2\text{Te}_3$  samples of various thicknesses were performed. Strong phonon activity and electron-phonon coupling were experimentally revealed and found to be sensitive to temperature changes and subtle structural variations between the samples. The experimental results, well described by Drude-Lorentz-Fano model, were compared to density functional theory calculations, yielding the phonon mode assignment. Further, an additional broadened background absorption was observed and attributed to the morphology of the conductive top surface of the samples.

DOI: [10.1103/y1qg-vjnz](https://doi.org/10.1103/PhysRevB.112.214303)

## I. INTRODUCTION

Three-dimensional topological insulators (TIs) feature graphene-like gapless surface states of massless Dirac fermions with (quasi)linear energy-momentum dispersion. Meanwhile, the bulk resembles a trivial semiconductor, characterized by gapped valence and conduction bands, with conventional massive Schrödinger electrons [1–6]. The Dirac electrons of the surface states are spin-momentum locked owing to strong spin-orbit coupling and are protected by time-reversal symmetry, and are consequently immune to elastic backscattering. They further exhibit quantum interference with bulk phonons [7–10]. Similar to graphene, the TIs show remarkably strong optical nonlinearity when interacting with moderately intense light fields, particularly in the terahertz (THz) frequency range, and additionally possess even-order nonlinearity, which is absent in the centrosymmetric graphene [11–14]. These unique characteristics open pathways for a broad range of applications of topological insulators in advanced technologies, including spintronics,

quantum computing, optoelectronics, frequency multipliers, and thermoelectrics [2,15–20].

Among this promising class of materials, the binary TIs  $\text{Bi}_2\text{Se}_3$ ,  $\text{Bi}_2\text{Te}_3$ , and  $\text{Sb}_2\text{Te}_3$  are the most extensively studied [1–20]. However, alloying these materials to form ternary compounds such as  $(\text{Bi}_{1-x}\text{Sb}_x)_2\text{Te}_3$  and  $\text{Bi}_2(\text{Se}_x\text{Te}_{1-x})_3$ , allows one to control the physical properties of TIs. Controlling the concentration *x* of the substituent element in these alloys allows to tune the bulk bandgap energy, the Fermi level and the relative energy of the Dirac point of the surface states to the band edges of the bulk bands, and the electron-phonon interactions [21–24]. Moreover, the inclusion of indium to form  $(\text{Bi}_{1-x}\text{In}_x)_2\text{Se}_3$  can control the spin-orbit coupling, enabling the recovery of a trivial insulator [8,25]. Given that the lowest energy optical phonons and the major spectral weight of the free electron conduction in TIs lie in the THz frequency range, THz [7,8,10,24–27] and Raman [28–30] spectroscopies are ideal tools to study the electron and phonon dynamics and their interactions in these materials.

Here, we study the electron and phonon dynamics as well as the electron-phonon interactions and their dependencies on the lattice temperature in the ternary topological insulator  $(\text{Bi}_{1-x}\text{Sb}_x)_2\text{Te}_3$  at THz frequencies. Our experiments provide conductivity spectra which we attribute to surface free charge carriers and optical phonon resonances. Interestingly, the free carrier conductivity obtained from the THz time-domain spectroscopy (THz-TDS) experiments shows no variation with the change of the lattice temperature while the phonon resonances exhibit drastic changes in lineshape, intensity, linewidth and central frequency. These features are all captured by a

\*Contact author: [hafez@physik.uni-bielefeld.de](mailto:hafez@physik.uni-bielefeld.de)

†Contact author: [dmtu@physik.uni-bielefeld.de](mailto:dmtu@physik.uni-bielefeld.de)

Drude-Lorentz-Fano model, very well reproducing the experimental data. Supported by the density functional theory (DFT) calculations, we attribute the IR-active phonons probed by the THz-TDS mainly to  $E_u$  modes associated with lattice vibrations in the (001) plane. On the other hand, the Raman spectra show signatures of  $E_g$  and  $A_g$  phonon modes. The intensities and central frequencies of the probed phonon modes are found to be sensitive to small structural variations from one sample to another, and are further highly sensitive to temperature changes. The conduction by free electrons at low temperatures below  $\sim 25$  K can plausibly be attributed to surface Dirac electrons, while the bulk electrons contribution is reasonably negligible. However, at higher temperatures, the strong THz phonon absorption and its associated temperature-induced broadening make it challenging to accurately assess the free electron conduction from the THz spectra alone. To this end, we have additionally performed contact-based electrical transport measurements, which are solely sensitive to free carrier conduction at dc.

## II. EXPERIMENTS

We performed the THz-TDS and Raman spectroscopy experiments on three samples of  $(\text{Bi}_{1-x}\text{Sb}_x)_2\text{Te}_3$  with thicknesses of  $\sim 23$  nm,  $\sim 27$  nm, and  $\sim 34$  nm, each deposited on a 0.5-mm-thick sapphire substrate [see Methods (Sec. V) for the samples preparation]. A bare piece of nominally identical sapphire substrate was used as a reference for control measurements. The THz-TDS experiments were performed in a transmission geometry using a commercial THz spectrometer (TeraFlash Pro from Toptica Photonics AG). The measurements at temperatures in the range 10–300 K were enabled by a closed-cycle helium cryostat with the samples mounted on its cold arm. The THz beam was focused at the sample position, and all measurements were conducted at normal incidence. The THz beam path was continuously purged with dry nitrogen to minimize the THz absorption by atmospheric water vapor. The useful bandwidth of the THz-TDS experiments was 0.3–3.5 THz, limited in part by the transmission of the TPX cryostat windows. The THz conductivity spectra of each sample were obtained by analyzing the temporal THz fields  $E_s(t)$  and  $E_{\text{ref}}(t)$  transmitted through the sample and the bare reference substrate, respectively, using the following relation [31–33]:

$$\tilde{\sigma}(\omega) = \frac{n_s + 1}{Z_0 d_{\text{film}}} \left( \frac{\tilde{E}_{\text{ref}}(\omega)}{\tilde{E}_s(\omega)} e^{i(n_s-1)\omega\Delta d/c} - 1 \right), \quad (1)$$

where  $\omega$  is the angular frequency,  $n_s = 3.07$  is the refractive index of the sapphire substrate,  $Z_0 = 377 \, \Omega$  is the free-space impedance,  $d_{\text{film}}$  is the thickness of the  $(\text{Bi}_{1-x}\text{Sb}_x)_2\text{Te}_3$  nanofilm,  $\tilde{E}(\omega)$  is the complex-valued Fourier spectrum of  $E(t)$ ,  $c$  is the speed of light in vacuum, and  $\Delta d \approx 5 \, \mu\text{m}$  accounts for a small thickness difference between the sample and reference substrates. Three thin film thicknesses were chosen to compare the conductivity  $\tilde{\sigma}(\omega)$  of the samples and the associated phonon contribution for a varying thickness  $d_{\text{film}}$ .

TABLE I. EDX characterization of the three  $(\text{Bi}_{1-x}\text{Sb}_x)_2\text{Te}_3$  samples, indicating good agreement with the expected (BiSb):Te ratio and an  $x$  of 0.61–0.67. Values given in this table exhibit a maximum error of  $\pm 5\%$ .

Content/sample	S1: 23 nm	S2: 27 nm	S3: 34 nm
Bi (%)	10	12	14
Sb (%)	22	23	22
Te (%)	68	65	64

The crystalline quality and spatial uniformity of the three  $(\text{Bi}_{1-x}\text{Sb}_x)_2\text{Te}_3$  samples were evaluated via micro-Raman spectroscopy, x-ray diffraction spectroscopy (XRD), scanning electron microscopy (SEM), energy-dispersive x-ray spectroscopy (EDX), and EDX mapping, as discussed in more detail in the next sections. The stoichiometry obtained by EDX characterization is shown in Table I. Electrical transport measurements, including Hall (up to  $\pm 8$  T) and temperature-dependent resistance measurements, were performed with the samples directly after the preparation, as discussed in more detail in Methods (Sec. V). A comparison between the results obtained from the THz spectroscopy and electrical transport measurements is provided in the next section.

## III. RESULTS AND DISCUSSION

Figure 1 shows the THz spectra of the real and imaginary parts of the conductance [the product  $\tilde{\sigma}_s(\omega) = \tilde{\sigma} d_{\text{film}}$  in Eq. (1)] for the three studied samples at different temperatures. Colored curves and solid lines show the experimental data and Drude-Lorentz-Fano model fitting, respectively. The model fitting, which we shall discuss in detail below, shows very good agreement with the data. The conductance spectra possess a finite dc conductance and clear signatures of IR-active phonons. The peak and lineshape of the phonon mode centered around 1.5 THz at the temperature of 300 K exhibit a strong dependence on the sample temperature. With the reduction of temperature, we see an increase of the peak amplitude, red-shift (anomalous mode softening on cooling) and linewidth narrowing. This anomalous mode softening on cooling (or equivalently, mode hardening on heating) has been previously observed in the TIs and has been attributed to the strong electron-phonon interactions and higher-orders mode anharmonicity [10,25,34]. In contrast, the broader, higher-frequency peak around 1.9 THz exhibits only a slight red-shift on cooling. We note here that similar phonon signatures have been observed in Sn-doped  $\text{Bi}_{1.1}\text{Sb}_{0.9}\text{Te}_2\text{S}$  [10], comprising a sharp peak around 1.92 THz ( $64 \, \text{cm}^{-1}$ ), referred to as in-plane IR-active  $\alpha$ -mode, and a higher frequency shoulder presumably attributed to out-of-plane modes activated by lattice disorder (see [10] and references therein).

In order to describe the measured THz conductivity spectra shown in Fig. 1, we applied a fitting based on the following Drude-Lorentz-Fano model function [7,8,10,25,35–39], which provided a very good agreement with the data, as

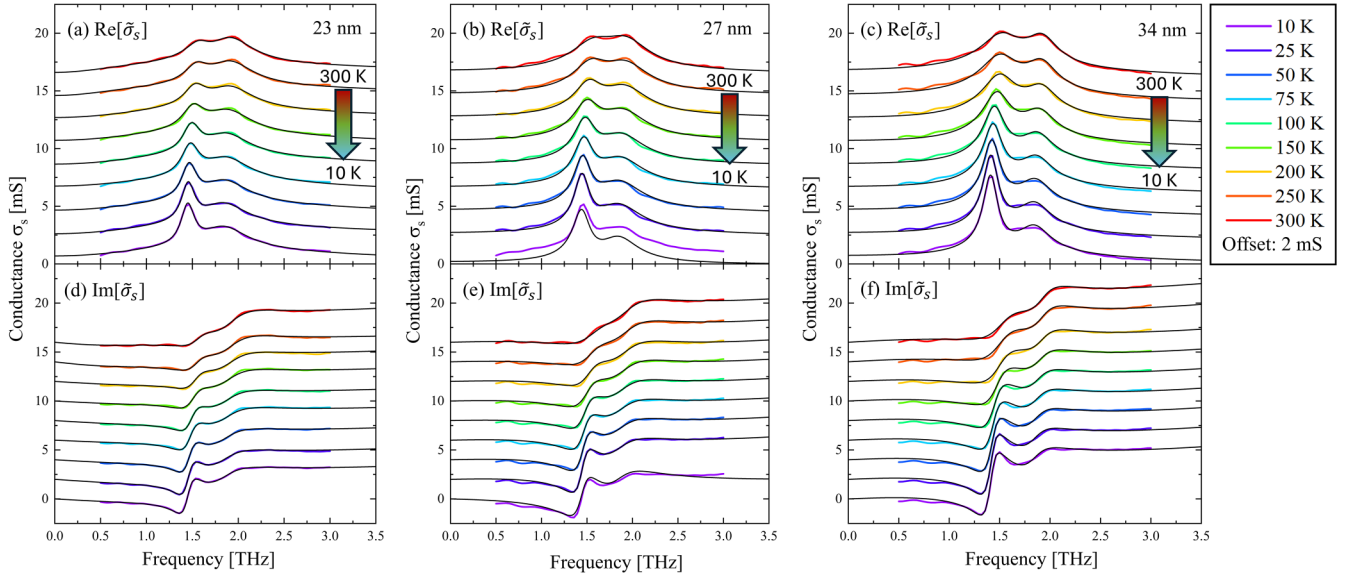


FIG. 1. The real (a)–(c) and imaginary (d)–(f) parts of the complex-valued sheet conductance spectra for the three investigated samples at temperatures between 10 K and 300 K. An offset by 2 mS between each two successive spectra is added for clarity. The black lines depict the Drude-Lorentz-Fano fits, while the colored spectra represent the experimental data.

shown in Figs. 1 and 2,

$$\begin{aligned} \tilde{\sigma}(\omega) = & \frac{\sigma_{dc}}{1 - i\omega\tau} + \frac{-i\epsilon_0\omega\Omega_1^2}{\omega_{0,L1}^2 - \omega^2 - i\gamma_{L1}\omega} + \frac{-i\epsilon_0\omega\Omega_2^2}{\omega_{0,L2}^2 - \omega^2 - i\gamma_{L2}\omega} \\ & + (-i\epsilon_0\omega)R \left[ \frac{\Gamma}{\Gamma^2 + \Delta\omega^2} (2q\Gamma - \Delta\omega(q^2 - 1)) + i \left( \frac{(q + \frac{\Delta\omega}{\Gamma})^2}{1 + (\frac{\Delta\omega}{\Gamma})^2} - 1 \right) \right] - i\omega\epsilon_0(\epsilon_\infty - 1). \end{aligned} \quad (2)$$

In this function, the first term on the right-hand side accounts for Drude conductivity by free charge carriers, where  $\sigma_{dc}$  is the dc conductivity and  $\tau$  is the electron momentum scattering time. The second and third terms represent two Lorentzian resonant modes which we associate here with the broad band around 1.9 THz in Fig. 1, and we will discuss them in detail in the next sections. For these resonant modes,  $\Omega$  is the oscillator strength,  $\gamma$  is the linewidth, and  $\omega_{0,L}/2\pi$  is the central resonance frequency. The fourth term is a Fano function [35–39], employed here to describe an asymmetry in the lineshape of the sharp peak around 1.5 THz in Fig. 1, where  $q$  is the asymmetry Fano parameter,  $R$  is a factor accounting for the rate of transition between continuum and discrete states, and  $\Delta\omega = \omega - \omega_{0,F}$  with  $\omega_{0,F}/2\pi$  the resonance frequency of the mode. This Fano function accounts for the quantum interference between the phonon discrete states and the free electron continuum, where the most pronounced asymmetry of the phonon lineshape arises when  $q = 0$ , such that the coupling of the phonon mode to the driving light field is minimum. In the last term of Eq. (2),  $\epsilon_0$  is the permittivity of free-space and  $\epsilon_\infty$  is the high-frequency dielectric constant. The individual contribution of each term of Eq. (2) to the overall conductance spectrum is depicted in Figs. 2(a)–2(d). The fit parameters used in Eq. (2), and their temperature dependencies are summarized in Table II and Fig. 3. We emphasize here that the inclusion of all components given in

Eq. (2) is essential for accurately reproducing the experimental conductivity spectra.

To get deeper insights into the fitting results and correctly assign the resonance modes observed in the conductivity spectra, we have first performed DFT calculations to investigate the possible phonon modes in the  $(\text{Bi}_{1-x}\text{Sb}_x)_2\text{Te}_3$  films. From the DFT calculations [see Methods (Sec. V) for details], we assign the experimentally observed resonances to the IR-active phonon modes demonstrated in Figs. 2(e) and 2(f) for a calculation of  $\text{BiSbTe}_3$  (based on structure mp-1227340

TABLE II. Temperature-independent Drude-Lorentz-Fano fit parameters used for the global fit.

Parameter/sample	S1: 23 nm	S2: 27 nm	S3: 34 nm
$\omega_{0,L1}/2\pi$ [THz]	$1.61 \pm 0.03$	$1.6 \pm 0.3$	$1.60 \pm 0.05$
$\Omega_{L1}$ [THz]	$244 \pm 8$	$100 \pm 30$	$160 \pm 20$
$\Omega_{L2}$ [THz]	$187 \pm 7$	$190 \pm 10$	$130 \pm 10$
$\gamma_{L1}$ [ps <sup>-1</sup> ]	$16 \pm 4$	$10 \pm 5$	$8 \pm 1$
$\gamma_{L2}$ [ps <sup>-1</sup> ]	$3.8 \pm 0.1$	$3.8 \pm 0.2$	$2.4 \pm 0.1$
$R$	$3 \pm 2$	$30 \pm 40$	$4 \pm 6$
$\epsilon_\infty$	$\approx 1 \pm 10^{-6}$	$\approx 1 \pm 10^{-6}$	$\approx 1 \pm 10^{-6}$
$E_F$ [meV]	$140 \pm 10$	$210 \pm 40$	$80 \pm 20$
$N_e \times 10^{12}$ [cm <sup>-2</sup> ]	$1.8 \pm 0.1$	$4 \pm 1$	$0.6 \pm 0.1$

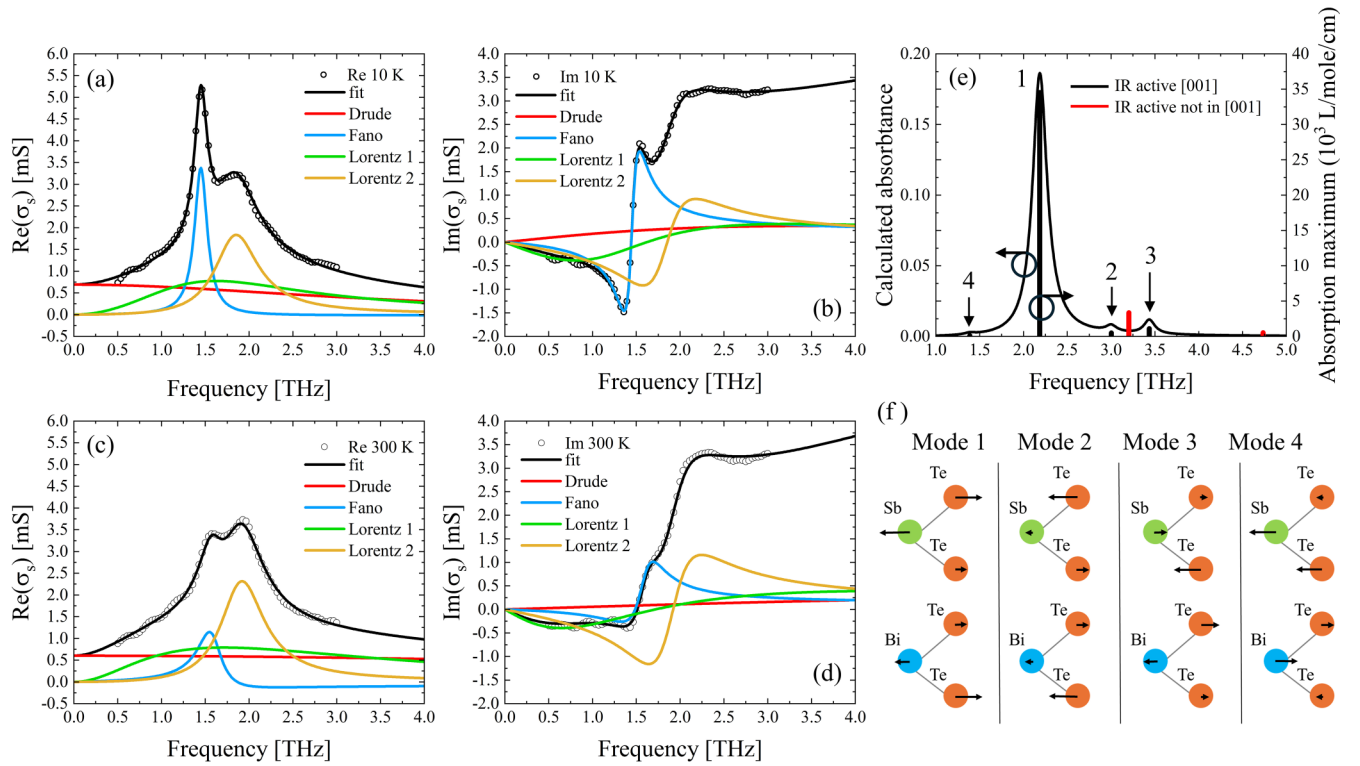


FIG. 2. (a)–(d) The Drude-Lorentz-Fano fits of the THz conductance along with their individual contributions for the 23-nm-thick sample (S1) at 10 K (a), (b) and 300 K (c), (d). In black, the experimental data are represented by symbols and the overall fitting is demonstrated by solid lines. The individual fitting contributions are represented by red for the Drude contribution, blue for the Fano contribution while green and orange correspond to the double-phonon band represented by the Lorentz functions of Eq. (2) with the broad Lorentzian (Lorentz 1) necessary to model the shoulder and sharp phonon feature accurately. (e) Shows the DFT simulation based on harmonic potentials, depicting the IR-active modes between 1 THz and 5 THz with  $5 \text{ cm}^{-1}$  FWHM absorbing in the (001) plane. (f) Schematic illustration of the atomic motions forming the vibrational modes 1–4, with the arrow's length indicative of the vibration strength.

taken from the materials project [40], which belongs to the trigonal space group R3m and the  $C_{3v}$  point group, lacking a center of inversion). Figure 2(e) shows the calculated spectral distribution of the (001) face (primitive unit cell) with both the E (black) and  $A_1$  (red) IR-active modes shown as vertical lines. Importantly, only the E modes contribute to the THz spectral response for this orientation of crystalline film. The corresponding atomic motions forming these modes are demonstrated schematically in Fig. 2(f). Correlating the DFT calculations to the experimental observations, we assign mode 1 to the experimentally observed peak around 1.5 THz, and modes 2 and 3 to the broader peak around 1.9 THz, which are mainly captured by the third and fourth terms (Lorentz 2 and Fano functions, respectively) of Eq. (2). The predicted mode 4 indicated in Fig. 2(e) is notably weak, and is likely masked in the measurements by both the more intense neighboring phonon modes and the free carrier absorption (the Drude conductance). We note that the results of the DFT calculations are qualitatively in good agreement with the experimental observations, except for a certain blue-shift in all the calculated central frequencies. This frequency shift is common in DFT calculations based on the harmonic-oscillator potentials and ideal stoichiometric lattice structure, where anharmonicity and lattice imperfections are not considered [25,41]. Further information about the DFT calculations is provided in Methods (Sec. V).

We note that replacing the Fano function term in Eq. (2) by a Lorentz function results in a less satisfactory agreement between the model and the data, especially for the thickest sample of 34-nm-thick film (see a comparison between results obtained from fitting with separate Fano and Lorentz functions in Methods.). This demonstrates that increasing the thickness of the sample results in a more pronounced phonon mode asymmetry. We also observe that this Fano-shaped mode around 1.5 THz exhibits an increase of intensity with increase of the sample thickness [see Figs. 1(a)–1(c)]. These observations indicate the significance of coupling between the free electron continuum of the surface states and the bulk phonons, described by the Fano term in Eq. (2). We also emphasize that the inclusion of all components in Eq. (2) is essential for accurately reproducing the experimental spectra.

Our investigation of the broad Lorentzian spectrum labeled “Lorentz 1” in Fig. 2, which is represented by the second term in Eq. (2), suggests that it does not correspond to a specific, well-resolved phonon mode. Instead, it represents a collective broadened background absorption arising likely from the following possible contributions combined. The surface can exhibit phonon absorption at the same resonance frequencies as bulk modes represented by the Fano and Lorentz 2 contributions shown in Figs. 2(a)–2(d) and in Eq. (2). However, unlike the crystalline bulk, the surface exhibits roughness of  $\sim 3 \text{ nm}$  on average and grains with a length of



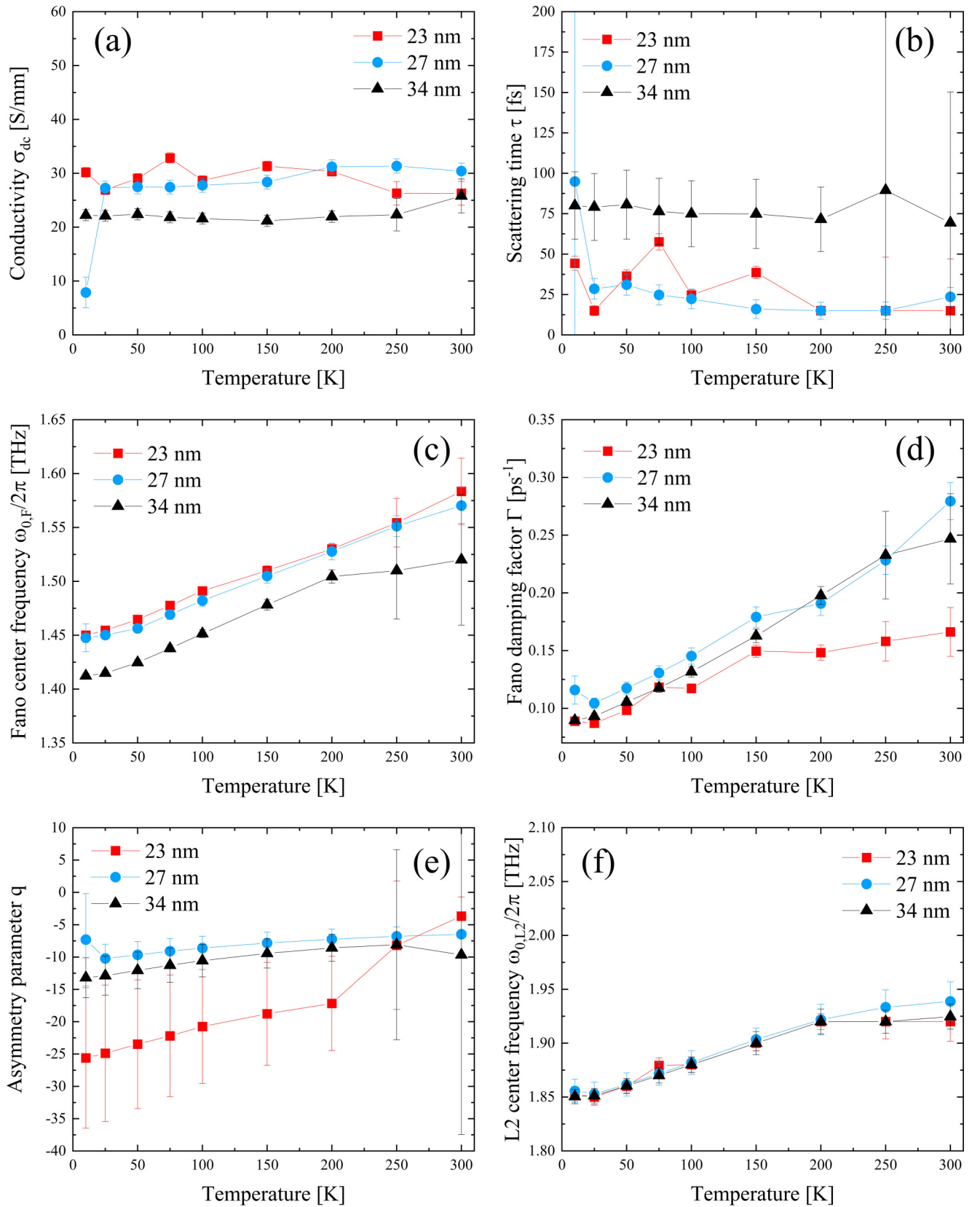


FIG. 3. The temperature dependence of the free fitting parameters of the Drude-Lorentz-Fano model for the three samples: (a) dc conductivity, (b) scattering time, (c) Fano center frequency, (d) Fano damping factor, (e) asymmetry  $q$  parameter, and (f) center frequency of the second Lorentzian term of Eq. (2).

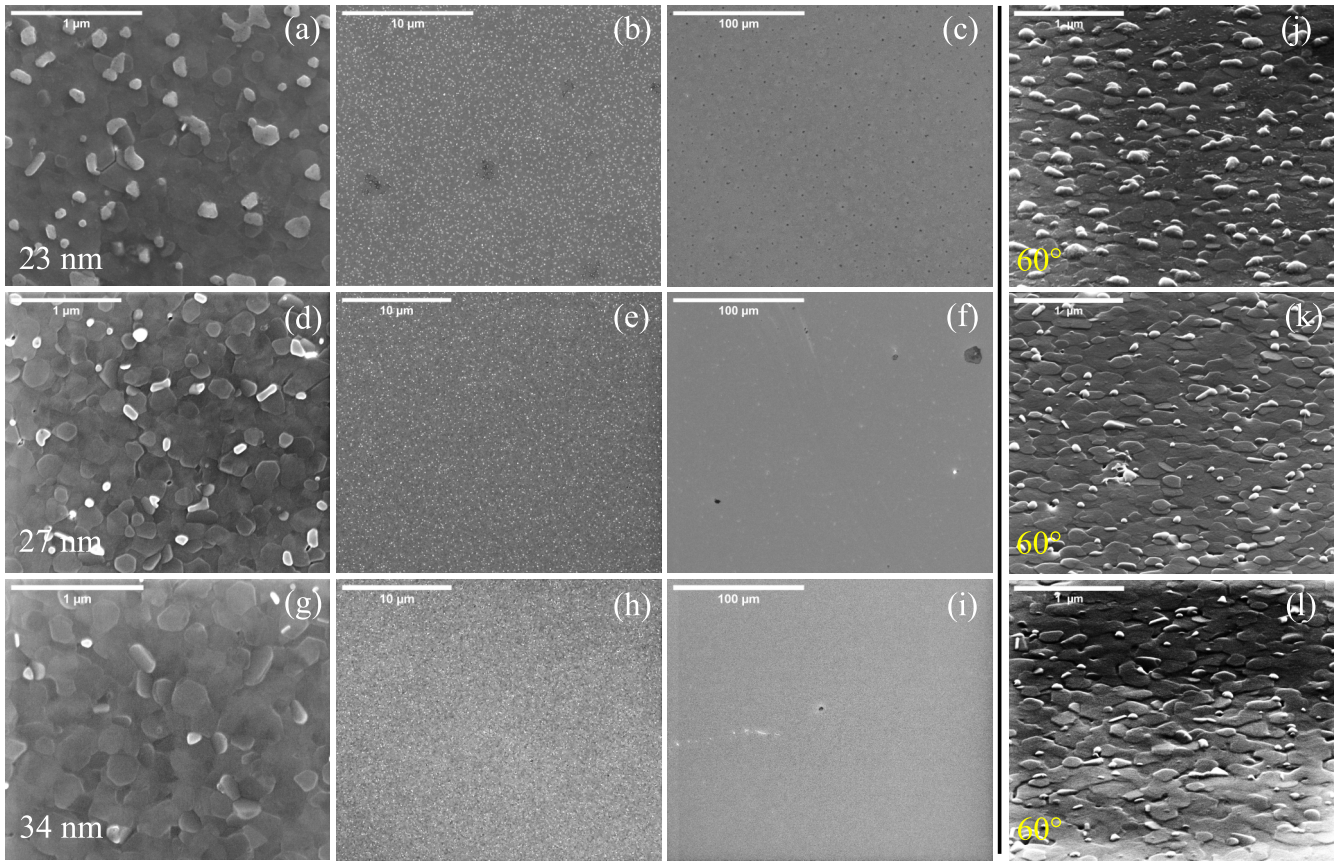


FIG. 4. SEM images of S1 (a)–(c), S2 (d)–(f) and S3 (g)–(i) with increasing scale of 1, 10, and 100  $\mu\text{m}$ . (j)–(l) 60° angled sample images showing sub- $\mu\text{m}$  grains and incomplete growth of the top 2–3 layers.

$\sim 140 \pm 70$  nm located within the top 2–3 layers of the  $(\text{Bi}_{1-x}\text{Sb}_x)_2\text{Te}_3$  films. This is depicted by the SEM images of the surface morphology shown in Fig. 4, and data demonstrated in Fig. 5 and Table III [see also Methods (Sec. V) for SEM characterization]. This amorphous nature of the surface can consequently result in a broadening of the surface phonon

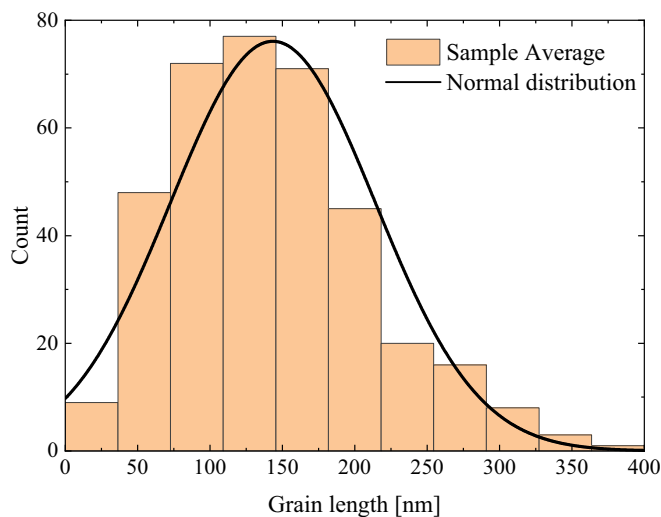


FIG. 5. Histogram representation of the distribution of the grain sizes demonstrated in Fig. 4 and Table III.

modes. Moreover, the surface grains, with their broad range of sizes and varying spatial distribution, can act as multiple THz plasmonic cavities that trap electron plasmonic waves [7,42–44], giving rise to additional broad THz absorption while suppressing dc conductivity.

Additional insights into the phonon activity in the samples can be obtained from the Raman spectra shown in Fig. 6. Raman-active vibrational modes were excited using a 532 nm Nd:YAG laser, focused to a  $\sim 2$   $\mu\text{m}$  spot with an optical power density of  $\sim 0.8$   $\text{mW}/\text{cm}^2$ . Spatial maps of the Raman response were recorded across the full sample surfaces to assess homogeneity. While the THz-TDS measurements indicate a largely homogeneous response due to the large spot size of the THz beam on the sample surface, Raman mapping with  $\sim 2$   $\mu\text{m}$  spot size reveals local variations in intensity and peak positions, as shown in Figs. 6(c) and 6(d), reflecting the grainy

TABLE III. Mean grain size obtained from SEM images Figs. 4(a), 4(d), and 4(g).

Sample	Mean length [nm]
S1: 23 nm	$140 \pm 70$
S2: 27 nm	$140 \pm 60$
S3: 34 nm	$160 \pm 80$
Average	$140 \pm 70$

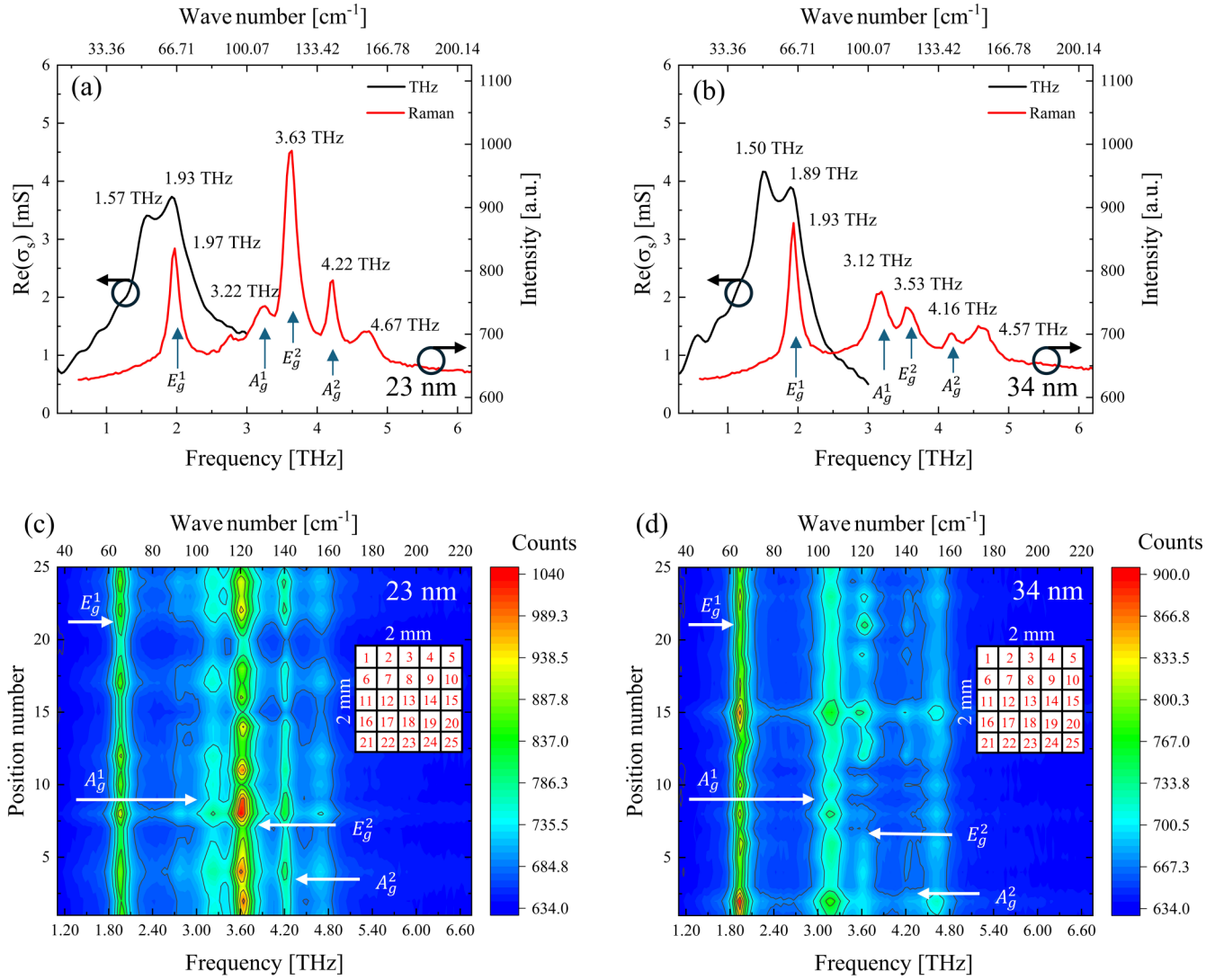


FIG. 6. (a), (b) Comparison between the IR-active and Raman-active modes for the two tested samples S1 and S3, and (c), (d) show a Raman mapping of the surface of each sample. The 2D Raman maps were extracted by combining the spectra recorded on 25 discrete points uniformly distributed over the  $1 \times 1 \text{ cm}^2$  sample surface, filling a grid with 2-mm spacing between the map spots, as illustrated by the sample map layouts shown in (c) and (d). Each Raman curve was acquired with the help of a 100X objective (Horiba Explora Plus), using a  $\sim 2\text{-}\mu\text{m}$ -diameter laser spot, with optical power density of  $\sim 0.8 \text{ mW}/\text{cm}^2$ .

surface morphology ( $\sim 3 \text{ nm}$  roughness and  $\sim 140 \text{ nm}$  mean grain length) observed in SEM and XRD. These variations also reflect the broad absorption spectrum represented by *Lorentz 1* in the THz fits.

To visualize the differences between the Raman-active and IR-active modes, we plotted the THz conductivity and Raman spectra together, for two of the samples. The Raman spectra show the predicted Raman-active  $E_g$  and  $A_{1g}$  modes [30]. To the best of our knowledge, this is an experimental observation of the theoretically predicted  $E_g^1$  mode centered around  $\sim 1.9 \text{ THz}$  ( $65 \text{ cm}^{-1}$ ) in  $(\text{Bi}_{1-x}\text{Sb}_x)_2\text{Te}_3$  [30]. We note here that in the DFT calculations, the considered structure has the stoichiometric ratio of  $\text{Bi} : \text{Sb} = 1 : 1$ , and lacks a center of inversion. Consequently, the calculated E and  $A_1$  modes lack a strict symmetry and are both IR- and Raman-active. In Fig. 6, however, we use the traditional labels for mode assignment, as also reported in Ref. [30], which imply a structure with a center of inversion. This can be justified by the observed

deviation of the actual structure of our samples, as described in Table I, from the aforementioned 1:1 ratio considered in the DFT calculations.

Based on the discussion provided above, we focus now on the findings of our fitting model given by Eq. (2) and the temperature dependence of the THz conductivity spectra. The best agreement with the experimental data of the THz conductance spectra shown in Figs. 1 and 2(a)–2(d) were obtained by considering the fitting parameters shown in Fig. 3 and Table II. For each sample, the parameters listed in Table II were fixed and did not change with the change of temperature. From the Drude term of Eq. (2), the dc conductance was extracted and was found almost independent of both temperature and sample thickness, as shown in Fig. 3(a). The associated electron momentum scattering time and the free electron density, however, vary only with the sample thickness, which we attribute to the structural variations of the samples demonstrated by the EDX data listed in Table I.



For the Fano function of Eq. (2), we demonstrate the temperature dependencies of the central frequency of the associated phonon mode  $\omega_{0,F}/2\pi$ , the linewidth  $\Gamma$ , and the Fano  $q$  parameter, as shown in Figs. 3(c)–3(e). The increase of  $\omega_{0,F}/2\pi$  and  $\Gamma$  with the increase of temperature indicate that the associated lattice potential becomes anomalously steeper (mode hardening on heating leading to a blue-shift). On the one hand, the negative finite values of the Fano  $q$  parameter denote a mode asymmetry with a dip on the high-frequency wing of the mode. On the other hand, the convergence of  $q$  towards zero with the increase of temperature results in a more pronounced asymmetry and a decrease of the coupling between the THz light field and the discrete states of this phonon mode, i.e., more continuum states become involved [10,38,45].

The broader band around 1.9 THz is represented in the performed fitting by the two Lorentzian functions in Eq. (2) whose central frequencies at 10 K are  $\omega_{0,L1}/2\pi = 1.6$  THz and  $\omega_{0,L2}/2\pi = 1.85$  THz. As discussed earlier,  $\omega_{0,L1}$  is associated with the broad background absorption labeled Lorentz 1 in Figs. 2(a)–2(d), which we attributed to a collective THz absorption from surface phonons and localized plasmonic absorption, all broadened by the surface morphology. The fitting results suggest that this part of absorption is not sensitive to the change of the sample temperature. Thus, the only temperature dependence of the broad band around 1.9 THz is likely attributed to a slight increase in the central frequency  $\omega_{0,L2}/2\pi$  from 1.85 THz to  $\sim 1.92$  THz with the increase of temperature from 10 K to 300 K, respectively. This indicates that the phonon mode associated with  $\omega_{0,L2}$  exhibits a small mode softening on cooling, similar to the case of the Fano mode. The other fitting parameters, however, do not show any change with temperature. This is evident because of the small intensity of this broad band around 1.9 THz as compared with the lower-frequency Fano mode whose temperature dependence is dominant. The narrowing of the Fano mode around 1.5 THz on cooling reduces the intensity at the neighboring broad band around 1.9 THz, counteracting any probable intrinsic increase of its peak on cooling, and therefore the overall result is the observed temperature independence of the broad band around 1.9 THz.

Assuming that the Drude contribution of the conductance is provided only by the Dirac electrons of the surface states, given that the samples are  $n$ -type TIs, we calculate the Fermi energy  $E_F$  and the areal free electron density  $N_e$  for each sample using the relation  $E_F = 2\hbar v_F \sqrt{\pi N_e} = \frac{\pi \hbar^2 \sigma_{s,dc}}{e^2 \tau}$  [6,26,46], where a factor of 2 accounts for two surfaces of a TI sample,  $\hbar$  is the reduced Planck's constant,  $v_F = 4.5(\pm 0.8) \times 10^5$  ms $^{-1}$  is the Fermi velocity [22,23], and  $\sigma_{s,dc} = \sigma_{dc} d_{\text{film}}$  is the dc conductance extracted from the THz conductance spectra shown in Fig. 1. The obtained values for  $E_F$  and  $N_e$  are listed in Table II. Our assumption of considering free electron conduction solely by surface electrons is motivated by the following. First, our samples are  $n$ -type, according to the Hall effect measurements performed. Second,  $(\text{Bi}_{1-x}\text{Sb}_x)_2\text{Te}_3$  exhibits a bulk bandgap of  $\sim 250$  meV, and the Dirac point of the surface states is almost at the edge of the bulk valence band [21–23]. Hence, our THz spectroscopy-based estimates of the Fermi energies (see Table II) can be attributed mainly to

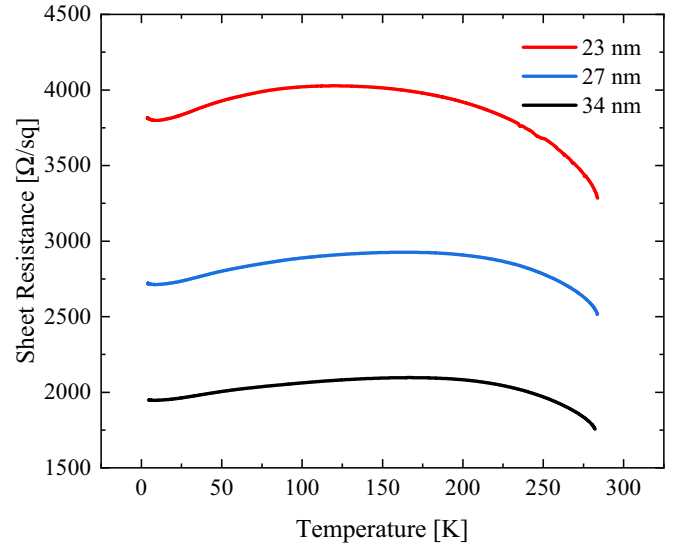


FIG. 7. Temperature dependence of the sheet resistance ( $R_s - R_{300\text{ K}}$ ) for the three samples.

free surface electron population. However, we realize a slight mismatch between the temperature dependencies of the electron transport properties extracted from the THz spectroscopy and those obtained from the contact-based electrical transport measurements demonstrated in Fig. 7 and Table IV.

At low temperatures below  $\sim 25$  K, the extracted values of the free carrier density from both methods are of the same order of magnitude and in reasonable agreement with one another. The slight differences between the values in this low-temperature regime can be attributed to the different sensitivities of the THz-TDS and the contact-based transport measurements to the different carrier scattering events [25,47].

At higher temperatures, on the contrary, the mismatch is more pronounced. Figure 7 shows the temperature dependence of the electrically measured sheet resistance exhibiting a fractional change of  $\sim 20\%$  with the temperature change from 10 K to 300 K, which is somewhat distinguished from the THz-based results shown in Fig. 3(a). The behavior shown in Fig. 7 is typical of contact-based transport characterization of  $(\text{Bi}_{1-x}\text{Sb}_x)_2\text{Te}_3$  for  $x \sim 0.5-0.9$  [22] and is attributed to interplay between contributions from surface and bulk bands [48]. In the low-temperature regime before the resistance peaks, the surface contribution dominates and exhibits an increase of resistance with the increase of temperature. At higher temperatures, the behavior is reversed, as captured in Fig. 7. Yet, the temperature at which the resistance reaches a maximum differs from one sample to another, most likely owing to the different Fermi energies and the small structural variations between the samples. This behavior is not fully captured by THz-TDS because the dominance of the phonon absorption modes and their temperature-induced spectral broadening in the THz conductance spectra obscure the weak Drude contribution from free electrons. Furthermore, the Drude contribution from surface-state electrons overlaps strongly with the broad absorption feature (Lorentz 1). Hence, the contact-based electrical transport



TABLE IV. The electron transport characteristics of the samples obtained from the Hall effect measurements performed at 2.2 K.

Sample	Thickness [nm]	Electron density [ $\times 10^{12} \text{ cm}^{-2}$ ]	Hall Mobility [ $\text{cm}^2 \text{ V}^{-1} \text{ s}^{-1}$ ]	Sheet resistance [ $\Omega \text{ sq}^{-1}$ ], $T = 300 \text{ K}$
S1: 23 nm	$22.9 \pm 0.4$	$6.29 \pm 0.06$	$262 \pm 3$	3285
S2: 27 nm	$27.1 \pm 0.4$	$6.96 \pm 0.07$	$331 \pm 3$	2515
S3: 34 nm	$33.7 \pm 0.3$	$10.3 \pm 0.1$	$311 \pm 3$	1756

characterization of the free electron conduction becomes indispensable at higher temperatures.

#### IV. CONCLUSIONS

We have studied the electron and phonon dynamics in the ternary topological insulator  $(\text{Bi}_{1-x}\text{Sb}_x)_2\text{Te}_3$  using THz-TDS, Raman spectroscopy, SEM imaging, and contact-based transport characterization methods. The THz conductivity spectra are dominated by strong THz-resonant phonon absorption modes featuring Fano-asymmetry owing to electron-phonon coupling, and further show strong dependencies on temperature and subtle structural variations in the samples. The IR-active modes were assigned using the DFT calculations, and significant phonon mode softening on cooling (phonon red shift at lower temperatures) was observed. The electrical conduction in the samples was found to be predominantly owing to the Dirac surface electrons states. An additional broad background absorption (or conductivity) overlapping the conductivity spectra of the samples was observed and attributed to absorption contribution induced by the morphology of the conductive top surface of the samples. This latter finding is supported by SEM imaging and XRR characterizations of the sample surfaces. A very good description of the complex THz optical conductivity spectra of the  $(\text{Bi}_{1-x}\text{Sb}_x)_2\text{Te}_3$  samples was achieved using the Drude-Lorentz-Fano model. The electron and phonon dynamics, along with their interactions revealed in this study, could provide important inputs for the thermoelectric applications of  $(\text{Bi}_{1-x}\text{Sb}_x)_2\text{Te}_3$ .

#### V. METHODS

*Samples preparation.* The samples were prepared within a solid-source MBE system, with a base pressure of  $\approx 10^{-10}$  mbar. They were grown on  $\text{Al}_2\text{O}_3$  (0001) substrates by codeposition of bismuth from a dual-filament Knudsen cell, antimony, and tellurium were evaporated from valved cracker sources. The growth was established in a two-step process, with a  $\sim 5$ -nm-thick nucleation layer deposited at  $150^\circ\text{C}$ , before the sample temperature was raised to the growth temperature of  $210^\circ\text{C}$ , where the rest of the film was grown. All sample temperatures were measured with a thermocouple attached to the sample manipulator. All the samples were grown under chalcogenide rich conditions, such that the tellurium flux is at least 20 times that of the total bismuth and antimony fluxes. This is essential to minimize the formation of chalcogenide vacancies [49], to guarantee that the correct phase of the topological insulator is grown [50] and to ensure that the growth rate is determined by the total bismuth and antimony fluxes [51]. The temperature of the tellurium cracker zone was held  $200^\circ\text{C}$  above the tellurium reservoir, resulting

in cracker zone temperatures between  $560^\circ\text{C}$  and  $565^\circ\text{C}$ . The antimony cracker temperature was  $900^\circ\text{C}$  and the Sb flux was kept constant across the growth of all samples, while the Bi flux partial pressure was fixed at  $3 \times 10^{-9}$  mbar. Finally, the samples were cooled under a tellurium flux at  $3^\circ\text{C}/\text{min}$  above  $180^\circ\text{C}$  to improve the surface quality and avoid residual tellurium on the surface.

*X-ray diffraction (XRD) characterization.* The samples were diced for characterization, and structural properties of the wafers were subsequently verified by XRD, using the Cu  $K\alpha$  ( $\lambda = 1.54056 \text{ \AA}$ ) source of a PANalytical X'Pert Pro MPD PW3040-60 diffractometer as shown in Fig. 8(a). The XRD measurements of the (0003) and (0006) film peaks confirm that all layers have a lattice constant of  $3.04 \pm 0.01 \text{ nm}$ , showing that all samples are of a similar stoichiometry and exhibit a high degree of crystallinity.

The sample thicknesses and roughnesses were evaluated using x-ray reflectivity measurements (XRR) as shown in Fig. 8(b). The three samples have a thickness of  $22.9 \pm 0.4 \text{ nm}$  (sample S1),  $27.1 \pm 0.4 \text{ nm}$  (sample S2), and  $33.7 \pm 0.3 \text{ nm}$  (sample S3) and all deposited layers have a surface roughness of  $3.4 \pm 0.2 \text{ nm}$  while the substrate roughness is estimated by the fit to be  $0.4 \text{ nm}$ .

*Scanning electron microscopy (SEM) surface imaging and energy dispersive x-ray (EDX) mapping.* The samples were imaged using a FEI Helios NanoLab 600i dual-beam FIB. The electron beam was operated at an accelerating voltage of  $10 \text{ kV}$ . SEM images were acquired at  $1$ ,  $10$ , and  $100 \mu\text{m}$  length scales to visualize grain size and sample topology, as shown in Figs. 4(a)–4(i). To enhance topographical contrast, the samples were additionally tilted to  $60^\circ$  during imaging, as seen in Figs. 4(j)–4(l). Incomplete growth of the top 2–3 layers results in the surface roughness detected by the XRR measurements.

For EDX mapping, the built-in SDD Apollo 10 detector was employed with an increased accelerating voltage of  $20 \text{ kV}$ . All samples exhibit large-scale homogeneous distributions of Bi, Sb, and Te, as shown in Fig. 9. In the SEM reference images, additional features attributed to impurities are visible, likely originating from environmental contamination such as carbon-based compounds or dust particles.

*Hall characterization.* The samples were patterned into Hall bars via optical lithography and chemical wet etching techniques before Cr/Au ohmic contacts were deposited by thermal evaporation. Transverse and longitudinal Hall resistances were subsequently recorded by standard lock-in techniques with a source-drain bias current of  $1 \mu\text{A}$  at a frequency of  $119.77 \text{ Hz}$  in a closed cycle helium cryostat with a base temperature of  $2.2 \text{ K}$  and a  $7 \text{ T}$  magnet. All samples show semiconductor-like behavior (as shown in Fig. 7) and

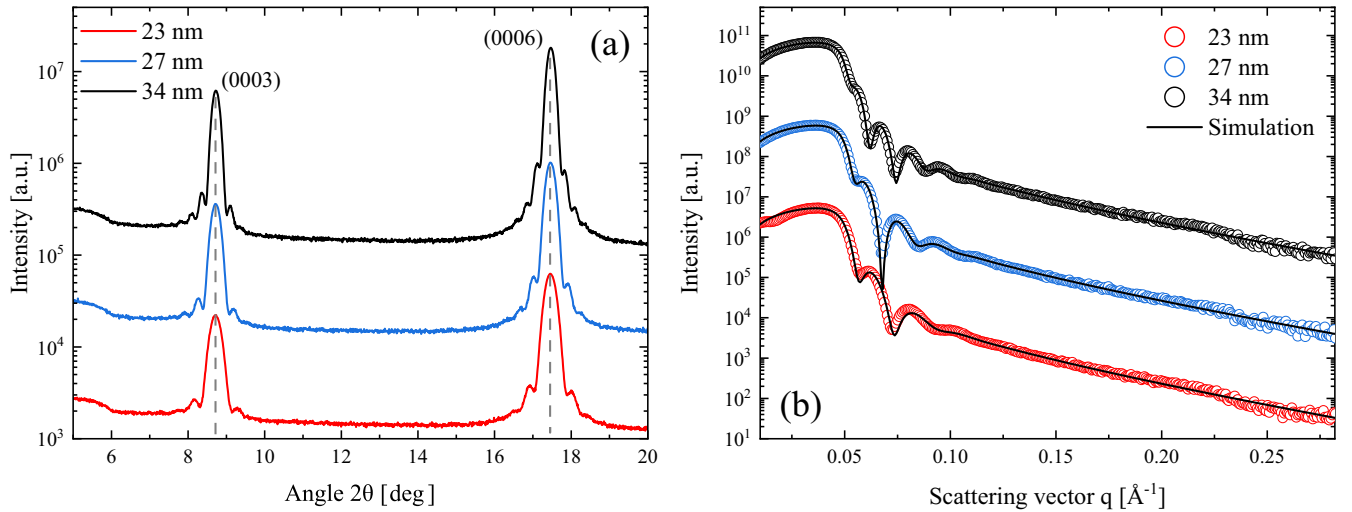


FIG. 8. Data of the (a) XRD and (b) XRR measurements for the three samples. A multiplicative offset of 10 (a) and 100 (b) between each two successive spectra is added for clarity.

transport dominated by electron-like carriers. The low-temperature transport properties of the samples studied here are reported in Table IV.

**DFT calculations.** Calculations were performed using VASP 5.4.4 [52] using the Perdew–Burke–Ernzerhof (PBE) functional [53] and the Projector Augmented Wave (PAW) pseudopotentials [54] distributed with VASP 5. Dispersion

corrections were included using the Grimme DFT-D3 method [55] with Becke–Johnson damping [56].

Within reasonable limits, the initial starting structure  $\text{BiSbTe}_3$  (mp-1227340), which is in an  $R3m$  space group, was taken from the materials project [40] and after some convergence testing both, geometry optimizations and phonon calculations were performed on a single unit cell in

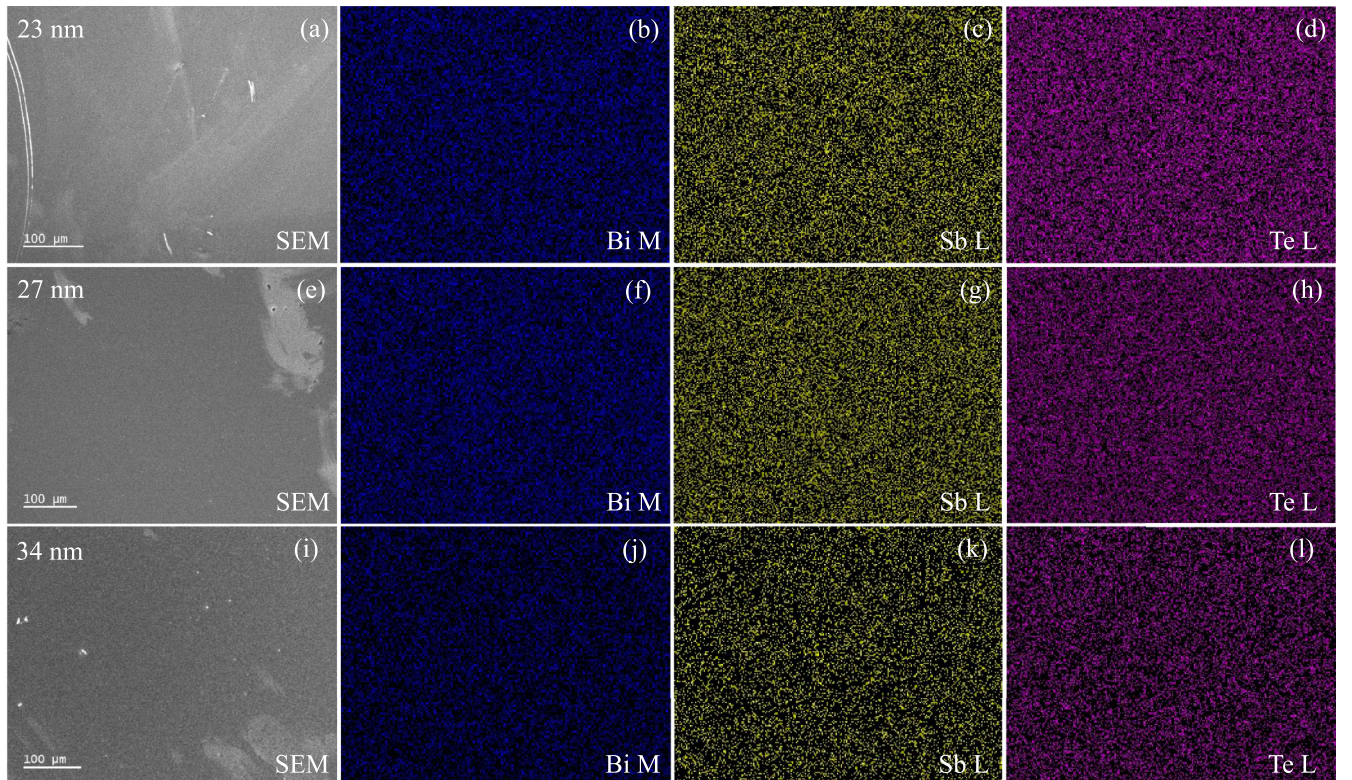


FIG. 9. EDX mapping with corresponding SEM images for the samples S1 (a)–(d), S2 (e)–(h), and S3 (i)–(l). The gray images (a), (e), (i) show reference SEM images. Blue images (b), (f), (j), yellow images (c), (g), (k), and purple images (d), (h), (l) correspond to the Bi, Sb, and Te distributions respectively.



the conventional crystallographic setting. Calculations were performed with an energy cut-off of 520 eV and a gamma centered Monkhorst-Pack grid [57,58]. The wavefunction, positions and unit cell dimensions were converged during optimization so that the energy changed by less than  $1 \times 10^{-4}$  eV. During the optimization, the unit cell volume decreased by  $\sim 7\%$  to 489.49 Å<sup>3</sup>. The shrinkage of the unit cell during optimization contributes to the calculated phonon frequencies being systematically higher than in the experiment.

A phonon calculation was then performed using Phonopy [59,60]. Here, the optimized unit cell was used to calculate atomic displacements that generated ten displaced structures. Single point calculations were then performed for each displaced structure with VASP as described above. Additionally, VASP was used to calculate the Born Effective charges of the non-displaced cell using the LEPSILON keyword. Phonon frequencies were then calculated using phonopy with the “PRIMITIVE\_AXIS” keyword used to wrap the phonon frequencies of the conventional cell onto the primitive crystallographic setting.

The phonon calculation and associated Born effective charges were then post processed using PDielec [41,61] with the most recent version of the code (v8.2.0) [62]. PDielec was then used to calculate the optical behavior of a 20 nm of BiSbTe<sub>3</sub> on a sapphire substrate layer with the incident beam normal to the (001) face (defined by the primitive crystallographic setting) an azimuthal angle of 0° and a full-width-half-maximum of 5 cm<sup>-1</sup> for P-polarized light. To calculate this, PDielec implements several methods to determine the optical properties of a multilayer material based on the pyGTM code [63] with a transfer matrix method similar to that described by Passler *et al.* [64] and a scattering matrix that has been implemented as described in the PyLlama software documentation [65]. Figure 2(e) in the main text shows the resultant absorbance spectra for the material.

*Fano versus Lorentz fit comparison.* To illustrate and justify the choice of the fitting functions, we compare the Fano and Lorentzian fits in Fig. 10. For the prominent mode around 1.5 THz, a Lorentzian fit overestimates the broad shoulder around 1.9 THz and fails to capture the observed asymmetry of the peak around 1.5 THz, whereas a Fano function reproduces both the peak position and the asymmetric lineshape accurately. This confirms that the Fano lineshape is necessary for this mode, reflecting interference between the discrete phonon and continuum electronic states.

In contrast, the broader band around 1.9 THz does not display significant asymmetry in the experimental data. A Lorentzian function provides a satisfactory fit without introducing additional free parameters, demonstrating that a simple Lorentzian is sufficient for these weaker modes. Using a Fano function for the 1.9 THz modes would increase the number of free parameters without improving the fit quality or physical interpretability.

Overall, this comparison validates our approach of using a Fano function only for the asymmetric 1.5 THz mode, while

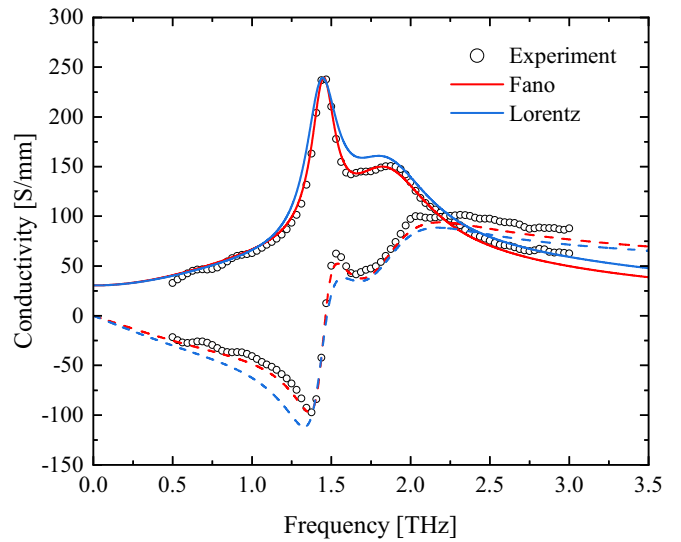


FIG. 10. Experimental data are shown as black dots. Drude-Fano-Lorentz is compared to a Drude-Lorentz model. The prominent 1.5 THz mode is fitted with a Fano function (red line, dashed for imaginary part) and a Lorentz function (blue line, dashed for imaginary part). The Lorentzian overestimates the right-hand shoulder and fails to reproduce the asymmetric lineshape, whereas the Fano function captures both the peak position and the asymmetry accurately.

fitting the 1.9 THz double-phonon band with Lorentzians is both physically justified and computationally efficient.

## ACKNOWLEDGMENTS

Group in Bielefeld acknowledges the financial support from the European Union’s Horizon 2020 research and innovation program (Grant Agreement No. 964735 EXTREME-IR), Deutsche Forschungsgemeinschaft (DFG) within Projects No. 468501411-SPP2314 INTEGRATECH and No. 518575758 HIGHSPINTERA, Bundesministerium für Bildung und Forschung (BMBF) within Project No. 05K2022 PBA Tera-EXPOSE, and Bielefelder Nachwuchsfonds. The authors acknowledge insightful discussions with Prof. Günter Reiss. Group in Leeds acknowledges the financial support from the European Union’s Horizon 2020 research and innovation program (Grant Agreement No. 964735 EXTREME-IR) and the UK EPSRC programme NAME (EP/V001914/1). CNR acknowledges the financial support from the European Union’s Horizon 2020 research and innovation program (Grant Agreement No. 964735 EXTREME-IR) the Italian Ministry of University and Research through the PNRR project PE0000023-NQSTI.

## DATA AVAILABILITY

The data that support the findings of this article are not publicly available. The data are available from the authors upon reasonable request.

[1] H. Zhang, C. X. Liu, X. L. Qi, X. Dai, Z. Fang, and S. C. Zhang, Topological insulators in Bi<sub>2</sub>Se<sub>3</sub>, Bi<sub>2</sub>Te<sub>3</sub> and Sb<sub>2</sub>Te<sub>3</sub> with a single Dirac cone on the surface, *Nat. Phys.* **5**, 438 (2009).

[2] D. Pesin and A. H. MacDonald, Spintronics and pseudospintronics in graphene and topological insulators, *Nat. Mater.* **11**, 409 (2012).



- [3] J. E. Moore, The birth of topological insulators, *Nature (London)* **464**, 194 (2010).
- [4] A. Anirban, 15 years of topological insulators, *Nat. Rev. Phys.* **5**, 267 (2023).
- [5] D. Hsieh, D. Qian, L. Wray, Y. Xia, Y. S. Hor, R. J. Cava, and M. Z. Hasan, A topological Dirac insulator in a quantum spin Hall phase, *Nature (London)* **452**, 970 (2008).
- [6] M. Z. Hasan and C. L. Kane, Colloquium: Topological insulators, *Rev. Mod. Phys.* **82**, 3045 (2010).
- [7] P. Di Pietro, M. Ortolani, O. Limaj, A. Di Gaspare, V. Giliberti, F. Giorgianni, M. Brahlek, N. Bansal, N. Koirala, S. Oh *et al.*, Observation of Dirac plasmons in a topological insulator, *Nat. Nanotechnol.* **8**, 556 (2013).
- [8] S. Sim, N. Koirala, M. Brahlek, J. H. Sung, J. Park, S. Cha, M. H. Jo, S. Oh, and H. Choi, Tunable Fano quantum-interference dynamics using a topological phase transition in  $(\text{Bi}_{1-x}\text{In}_x)_2\text{Se}_3$ , *Phys. Rev. B* **91**, 235438 (2015).
- [9] R. Heid, I. Y. Sklyadneva, and E. V. Chulkov, Electron-phonon coupling in topological surface states: The role of polar optical modes, *Sci. Rep.* **7**, 1095 (2017).
- [10] B. W. Li, W. C. Jiang, G. Y. Chen, Y. Xiang, W. Xie, Y. M. Dai, X. Y. Zhu, H. Yang, and H. H. Wen, Anomalous phonon softening in the topological insulator Sn-doped  $\text{Bi}_{1.1}\text{Sb}_{0.9}\text{Te}_2\text{S}$ , *Sci. China Phys. Mech. Astron.* **63**, 117011 (2020).
- [11] C. P. Schmid, L. Weigl, P. Grössing, V. Junk, C. Gorini, S. Schlauderer, S. Ito, M. Meierhofer, N. Hofmann, D. Afanasiev *et al.*, Tunable non-integer high-harmonic generation in a topological insulator, *Nature (London)* **593**, 385 (2021).
- [12] Y. Bai, F. Fei, S. Wang, N. Li, X. Li, F. Song, R. Li, Z. Xu, and P. Liu, High-harmonic generation from topological surface states, *Nat. Phys.* **17**, 311 (2021).
- [13] S. Kovalev, K.-J. Tielrooij, J.-C. Deinert, I. Ilyakov, N. Awari, M. Chen, A. Ponomaryov, M. Bawatna, T. V. A. G. de Oliveira, L. M. Eng *et al.*, Terahertz signatures of ultrafast Dirac fermion relaxation at the surface of topological insulators, *npj Quantum Mater.* **6**, 84 (2021).
- [14] F. Giorgianni, E. Chiadroni, A. Rovere, M. Cestelli-Guidi, A. Perucchi, M. Bellaveglia, M. Castellano, D. Di Giovenale, G. Di Pirro, M. Ferrario *et al.*, Strong nonlinear terahertz response induced by Dirac surface states in  $\text{Bi}_2\text{Se}_3$  topological insulator, *Nat. Commun.* **7**, 11421 (2016).
- [15] C.-K. Lee, J. H. Lee, B.-T. Zhang, and J.-L. He, Topological insulators and applications, in *2D Materials for Nanophotonics*, edited by Y. M. Jhon (Elsevier, Amsterdam, 2021), pp. 81–138.
- [16] X. Zhang, J. Wang and S. C. Zhang, Topological insulators for high-performance terahertz to infrared applications, *Phys. Rev. B* **82**, 245107 (2010).
- [17] M. Y. Toriyama and G. J. Snyder, Topological insulators for thermoelectrics: A perspective from beneath the surface, *The Innovation* **6**, 100782 (2025).
- [18] Q. Xia, Q. Xu, B. Xu, and L. Yi, *Ab initio* prediction of thermoelectric performance of monolayer  $\text{BiSbTe}_3$ , *J. Solid State Chem.* **296**, 121963 (2021).
- [19] D. Baldomir and D. Faflde, On behind the physics of the thermoelectricity of topological insulators, *Sci. Rep.* **9**, 6324 (2019).
- [20] T. Yang, Y. Yang, X. Wang, G. Zhang, and Z. Cheng, Topological thermoelectrics: New opportunities and challenges, *Mater. Today Chem.* **30**, 101488 (2023).
- [21] D. Kong, Y. Chen, J. J. Cha, Q. Zhang, J. G. Analytis, K. Lai, Z. Liu, S. S. Hong, K. J. Koski, S.-K. Mo *et al.*, Ambipolar field effect in the ternary topological insulator  $(\text{Bi}_x\text{Sb}_{1-x})_2\text{Te}_3$  by composition tuning, *Nat. Nanotechnol.* **6**, 705 (2011).
- [22] J. Zhang, C.-Z. Chang, Z. Zhang, J. Wen, X. Feng, K. Li, M. Liu, K. He, L. Wang, X. Chen *et al.*, Band structure engineering in  $(\text{Bi}_{1-x}\text{Sb}_x)_2\text{Te}_3$  ternary topological insulators, *Nat. Commun.* **2**, 574 (2011).
- [23] X. He, H. Li, L. Chen, and K. Wu, Substitution-induced spin-split surface states in topological insulator  $(\text{Bi}_{1-x}\text{Sb}_x)_2\text{Te}_3$ , *Sci. Rep.* **5**, 8830 (2015).
- [24] L. Wu, M. Brahlek, R. V. Aguilar, A. V. Stier, C. M. Morris, Y. Lubashevsky, L. S. Bilbro, N. Bansal, S. Oh, and N. P. Armitage, A sudden collapse in the transport lifetime across the topological phase transition in  $(\text{Bi}_{1-x}\text{In}_x)_2\text{Se}_3$ , *Nat. Phys.* **9**, 410 (2013).
- [25] C. S. Knox, M. T. Vaughan, A. D. Burnett, M. Ali, S. Sasaki, E. H. Linfield, A. G. Davies, and J. R. Freeman, Effects of structural ordering on infrared active vibrations within  $\text{Bi}_2(\text{Te}_{(1-x)}\text{Se}_x)_3$ , *Phys. Rev. B* **106**, 245203 (2022).
- [26] V. S. Kamboj, A. Singh, T. Ferrus, H. E. Beere, L. B. Duffy, T. Hesjedal, C. H. W. Barnes, and D. A. Ritchie, Probing the topological surface state in  $\text{Bi}_2\text{Se}_3$  thin films using temperature-dependent terahertz spectroscopy, *ACS Photonics* **4**, 2711 (2017).
- [27] B. C. Park, T. H. Kim, K. I. Sim, B. Kang, J. W. Kim, B. Cho, K. H. Jeong, M. H. Cho, and J. H. Kim, Terahertz single conductance quantum and topological phase transitions in topological insulator  $\text{Bi}_2\text{Se}_3$  ultrathin films, *Nat. Commun.* **6**, 6552 (2015).
- [28] V. Chis, I. Y. Sklyadneva, K. A. Kokh, V. A. Volodin, O. E. Tereshchenko, and E. V. Chulkov, Vibrations in binary and ternary topological insulators: First-principles calculations and Raman spectroscopy measurements, *Phys. Rev. B* **86**, 174304 (2012).
- [29] Y. Zhao, X. Luo, J. Zhang, J. Wu, X. Bai, M. Wang, J. Jia, H. Peng, Z. Liu, S. Y. Quek *et al.*, Interlayer vibrational modes in few-quintuple-layer  $\text{Bi}_2\text{Te}_3$  and  $\text{Bi}_2\text{Se}_3$  two-dimensional crystals: Raman spectroscopy and first-principles studies, *Phys. Rev. B* **90**, 245428 (2014).
- [30] R. R. Urkude and U. A. Palikundwar, Phonon dynamics of  $(\text{Bi}_{1-x}\text{Sb}_x)_2\text{Te}_3$  topological insulators by Raman spectroscopy, *Physica B* **655**, 414754 (2023).
- [31] R. E. Glover and M. Tinkham, Conductivity of superconducting films for photon energies between 0.3 and 40  $\text{kT}_c$ , *Phys. Rev.* **108**, 243 (1957).
- [32] P. U. Jepsen, D. G. Cooke, and M. Koch, Terahertz spectroscopy and imaging—Modern techniques and applications, *Laser Photon. Rev.* **5**, 124 (2011).
- [33] L. S. Bilbro, R. V. Aguilar, G. Logvenov, O. Pelleg, I. Božović, and N. P. Armitage, Temporal correlations of superconductivity above the transition temperature in  $\text{La}_{2-x}\text{Sr}_x\text{CuO}_4$  probed by terahertz spectroscopy, *Nat. Phys.* **7**, 298 (2011).
- [34] J. P. Heremans, R. J. Cava, and N. Samarth, Tetradymites as thermoelectrics and topological insulators, *Nat. Rev. Mater.* **2**, 17049 (2017).
- [35] R. P. S. M. Lobo, N. Bontemps, M. I. Bertoni, T. O. Mason, K. R. Poeppelmeier, A. J. Freeman, M. S. Park, and J. E. Medvedeva, Optical conductivity of mayenite: From insulator to metal, *J. Phys. Chem. C* **119**, 8849 (2015).

- [36] L. C. Davis and L. A. Feldkamp, Interaction of many discrete states with many continua, *Phys. Rev. B* **15**, 2961 (1977).
- [37] A. E. Miroshnichenko, S. Flach, and Y. S. Kivshar, Fano resonances in nanoscale structures, *Rev. Mod. Phys.* **82**, 2257 (2010).
- [38] M. F. Limonov, M. V. Rybin, A. N. Poddubny, and Y. S. Kivshar, Fano resonances in photonics, *Nat. Photon.* **11**, 543 (2017).
- [39] U. Fano, Effects of configuration interaction on intensities and phase shifts, *Phys. Rev.* **124**, 1866 (1961).
- [40] A. Jain, S. P. Ong, G. Hautier, W. Chen, W. D. Richards, S. Dacek, S. Cholia, D. Gunter, D. Skinner, G. Ceder *et al.*, Commentary: The materials project: A materials genome approach to accelerating materials innovation, *APL Mater.* **1**, 011002 (2013).
- [41] J. Kendrick and A. D. Burnett, PDielec: The calculation of infrared and terahertz absorption for powdered crystals, *J. Comput. Chem.* **37**, 1491 (2016).
- [42] W. Liu, L. Endicott, V. A. Stoica, H. Chi, R. Clarke, and C. Uher, High-quality ultra-flat BiSbTe<sub>3</sub> films grown by MBE, *J. Cryst. Growth* **410**, 23 (2015).
- [43] Z. Wang, T. P. Ginley, S. V. Mambakkam, G. Chandan, Y. Zhang, C. Ni, and S. Law, Plasmon coupling in topological insulator multilayers, *Phys. Rev. Mater.* **4**, 115202 (2020).
- [44] T. Stauber, G. Gómez-Santos, and L. Brey, Plasmonics in topological insulators: Spin-charge separation, the influence of the inversion layer, and phonon-plasmon coupling, *ACS Photonics* **4**, 2978 (2017).
- [45] N. Dean, J. C. Petersen, D. Fausti, R. I. Tobey, S. Kaiser, L. V. Gasparov, H. Berger, and A. Cavalleri, Polaronic conductivity in the photoinduced phase of 1T-TaS<sub>2</sub>, *Phys. Rev. Lett.* **106**, 016401 (2011).
- [46] C. S. Tang, B. Xia, X. Zou, S. Chen, H. W. Ou, L. Wang, A. Rusydi, J. X. Zhu, and E. E. M. Chia, Terahertz conductivity of topological surface states in Bi<sub>1.5</sub>Sb<sub>0.5</sub>Te<sub>1.8</sub>Se<sub>1.2</sub>, *Sci. Rep.* **3**, 3513 (2013).
- [47] N. A. Kabir, Y. Yoon, J. R. Knab, J. Y. Chen, A. G. Markelz, J. L. Reno, Y. Sadofyev, S. Johnson, Y. H. Zhang, and J. P. Bird, Terahertz transmission characteristics of high-mobility GaAs and InAs two-dimensional-electron-gas systems, *Appl. Phys. Lett.* **89**, 132109 (2006).
- [48] S. Shimizu, R. Yoshimi, T. Hatano, K. S. Takahashi, A. Tsukazaki, M. Kawasaki, Y. Iwasa, and Y. Tokura, Gate control of surface transport in MBE-grown topological insulator (Bi<sub>1-x</sub>Sb<sub>x</sub>)<sub>2</sub>Te<sub>3</sub> thin films, *Phys. Rev. B* **86**, 045319 (2012).
- [49] N. Bansal, Y. S. Kim, E. Edrey, M. Brahlek, Y. Horibe, K. Iida, M. Tanimura, G.-H. Li, T. Feng, H.-D. Lee *et al.*, Epitaxial growth of topological insulator Bi<sub>2</sub>Se<sub>3</sub> film on Si(111) with atomically sharp interface, *Thin. Solid. Films* **520**, 224 (2011).
- [50] A. Fülöp, Y. Song, S. Charpentier, P. Shi, M. Ekström, L. Galletti, R. Arpaia, T. Bauch, F. Lombardi, and S. Wang, Phase transition of bismuth telluride thin films grown by MBE, *Appl. Phys. Express* **7**, 045503 (2014).
- [51] S. Schreyeck, K. Brunner, A. Kirchner, U. Bass, S. Grauer, C. Schumacher, C. Gould, G. Karczewski, J. Geurts, and L. W. Molenkamp, Kinetic limitation of chemical ordering in Bi<sub>2</sub>Te<sub>3-x</sub>Se<sub>x</sub> layers grown by molecular beam epitaxy, *J. Phys.: Condens. Matter* **28**, 145002 (2016).
- [52] J. Hafner, Ab-initio simulations of materials using VASP: Density-functional theory and beyond, *J. Comput. Chem.* **29**, 2044 (2008).
- [53] J. P. Perdew, K. Burke, and M. Ernzerhof, Generalized gradient approximation made simple, *Phys. Rev. Lett.* **77**, 3865 (1996).
- [54] P. E. Blöchl, Projector augmented-wave method, *Phys. Rev. B* **50**, 17953 (1994).
- [55] S. Grimme, S. Ehrlich, and L. Goerigk, Effect of the damping function in dispersion corrected density functional theory, *J. Comput. Chem.* **32**, 1456 (2011).
- [56] A. D. Becke and E. R. Johnson, A density-functional model of the dispersion interaction, *J. Chem. Phys.* **123**, 154101 (2005).
- [57] H. J. Monkhorst and J. D. Pack, Special points for Brillouin-zone integrations, *Phys. Rev. B* **13**, 5188 (1976).
- [58] J. D. Pack and H. J. Monkhorst, Special points for Brillouin-zone integrations—A reply, *Phys. Rev. B* **16**, 1748 (1977).
- [59] A. Togo, L. Chaput, T. Tadano, and I. Tanaka, Implementation strategies in phonopy and phono3py, *J. Phys. Condens. Matter* **35**, 353001 (2023).
- [60] A. Togo, First-principles phonon calculations with phonopy and phono3py, *J. Phys. Soc. Japan* **92**, 012001 (2023).
- [61] J. Kendrick, <https://Github.Com/JohnKendrick/PDielec>, <https://github.com/JohnKendrick/PDielec>.
- [62] J. Kendrick, A. D. Burnett and Authorea-Committer, *JohnKendrick/PDielec: PDielec Version 8.2.0 Powder and Single Crystal Infrared Calculations*, <https://zenodo.org/records/14054801>.
- [63] M. Jeannin, <https://Pygtm.Readthedocs.io/En/Latest/>, <https://pygtm.readthedocs.io/en/latest/>.
- [64] N. C. Passler, M. Jeannin, and A. Paarmann, Layer-resolved absorption of light in arbitrarily anisotropic heterostructures, *Phys. Rev. B* **101**, 165425 (2020).
- [65] M. M. Bay, S. Vignolini, and K. Vynck, PyLlama: A stable and versatile Python toolkit for the electromagnetic modelling of multilayered anisotropic media, *Comput. Phys. Commun.* **273**, 108256 (2022).